

1 Controls on structural styles and decoupling in stratigraphic sequences
2 with double décollements during thin-skinned contractional tectonics:
3 insights from numerical modelling

4 Qingfeng Meng*¹, David Hodgetts

5 *School of Earth and Environmental Sciences, University of Manchester, M13 9PL, UK*

6 **Abstract**

7 Six series of particle-based numerical experiments were performed to simulate thin-skinned
8 contractional tectonics in stratigraphic sequences with double décollements during horizontal
9 shortening. The models were assigned with varying rock competence, depth and thickness of the
10 upper décollement, which resulted in significantly different styles of deformation and decoupling
11 characteristics above and below the upper décollement. The models composed of the least
12 competent material produced distributed sinusoidal detachment folds, with many shallow
13 structures profoundly decoupled from the deep-seated folds. The models composed of a more
14 competent material are dominated by faulted, diapir-cored box folds, with minor disharmonic folds
15 developed in their limbs. Differently, the results of models composed of the most competent
16 material are characterised by localised piggyback thrusts, fault-bend folds and pop-up structures
17 with tensile fractures developed in fold hinges. Depth of the upper décollements also plays an
18 important role in controlling structural decoupling, i.e. the shallower the upper décollements, the
19 higher the degree of decoupling becomes. Thicker upper décollements can provide sufficient
20 mobile materials to fill fold cores, and contribute to the formation of secondary disharmonic folds,
21 helping enhance structural decoupling. Our modelling results are comparable to the structural

¹ *Corresponding author. E-mail address: meng.qingfeng@hotmail.com

22 features exhibited in the Dezful Embayment of the Zagros Fold-and-Thrust Belt with the Miocene
23 Gachsaran Formation acting as the shallow upper décollement, and the Fars with the Triassic
24 Dashtak Formation as its intermediate décollement. This study demonstrates that rock competence,
25 depth and thickness of the upper décollements can jointly affect the structural styles and
26 decoupling. Our modelling results are instructive for structural interpretation of deep zones in fold-
27 and-thrust belts that exhibit distinct structural decoupling features.

28 **Key words**

29 structural decoupling; fold-and-thrust belt; décollement; discrete element; Zagros

30

31 **1. Introduction**

32 Thin-skinned deformation styles are typical of many fold-and-thrust (FAT) belts in the foreland of
33 a collisional zone (Chapple, 1978). In such systems, a basal weak layer (e.g. shale and evaporite)
34 serves as the main décollement that allows the deformed overburden to be detached on during
35 shortening (Davis and Engelder, 1985). Two or multiple décollements have been reported in many
36 FAT belts worldwide, such as the Apennines in Italy (Massoli et al., 2006; Tavani and Cifelli,
37 2010), the Jura in Switzerland (Sommaruga, 1999; Schori et al., 2015), the Salt Range in Pakistan
38 (Jaumé and Lillie, 1988; Gee and Gee, 1989), the Subandean in Bolivia (Leturmy et al., 2000;
39 Driehaus et al., 2014), the Kuqa in China (Wang et al., 2011; Izquierdo-Llavall et al., 2018), and
40 the Zagros in Iran (Seppehr et al., 2006), among others. The occurrence of multidécollements can
41 shape the variable geometry of FAT belts and affect forward propagation of deformation (Sherkati
42 et al., 2006; Ghanadian et al., 2017a). In particular, the deformation above and below the upper
43 décollement are commonly decoupled, which significantly increases structural complexity of the

44 systems and makes it difficult to unravel deep structures beneath the upper décollement (Derikvand
45 et al., 2018).

46

47 A thorough understanding of the styles of deformation and decoupling of FAT belts is crucial
48 partially due to their economic importance, given the fact that FAT belts constitute the most
49 prolific hydrocarbon provinces globally (Cooper, 2007). More fundamentally, this can yield
50 insights into the competing mechanisms for accommodation of thin-skinned shortening (Erickson,
51 1996), i.e. thrusting, folding and diapirism (Bonini, 2003; Najafi et al., 2018), and geologic
52 conditions required for coupling/decoupling of deformation. Extensive field and seismic based
53 observational studies (Sherkati et al., 2005; Casciello et al., 2009; Farzipour- Saein et al., 2009;
54 Fard et al., 2011; Vergés et al., 2011; Motamedi et al., 2012; Ghanadian et al., 2017b; Jahani et al.,
55 2017; Najafi et al., 2018; Derikvand et al., 2019), analogue modelling (Bahroudi and Koyi, 2003;
56 Sherkati et al., 2006; Konstantinovskaya and Malavieille, 2011; Driehaus et al., 2014; Ghazian
57 and Buitter, 2014; Santolaria et al., 2015; Farzipour-Saein and Koyi, 2016; Ghanadian et al., 2017c;
58 Borderie et al., 2018) and numerical modelling studies (Ruh et al., 2012, 2017; Feng et al., 2015)
59 have been conducted to address questions in FAT belts with double or multiple décollements. It
60 has been realized that rock mechanical properties (Dean et al., 2013; Morgan, 2015; Meng and
61 Hodgetts, 2019), décollements depth (Sepehr et al., 2006; Sherkati et al., 2006; Motamedi et al.,
62 2012) and thickness (Stewart, 1996, 1999; Costa and Vendeville, 2002; Meng and Hodgetts, 2019)
63 can determine the structural styles and decoupling in the shallow and deep segments of FAT belts.
64 Nevertheless, a more comprehensive study of the combined impact of these parameters is needed.

65

66 This study reports a numerical modelling study of thin-skinned tectonics in FAT belts, with
67 varying rock mechanical competence, thickness and depth of the upper décollement. The aims are
68 1) to produce realistic geologic structures comparable to natural examples; 2) to examine the
69 controls on structural styles and the competing mechanisms for shortening accommodation in FAT
70 belts with two dominant décollement levels; to 3) to investigate the role of the upper décollement
71 in structural decoupling above and below the upper décollement. Notably, some other factors, such
72 as existence of pre-existing structures (Callot et al., 2012), mechanical stratigraphy (Sepehr et al.,
73 2006; Farzipour-Saein et al., 2009), basal décollement thickness ((Bahroudi and Koyi, 2003; Meng
74 and Hodgetts, 2019), synkinematic sedimentation (Driehaus et al., 2014) and crustal shortening
75 rate (McQuarrie, 2004), can also play an important role in structural development of a thin-skinned
76 FAT belts with two or multiple décollements; however, this is beyond the scope of the current
77 study. The modelling results presented here exhibit first-order structural similarities to the Fars
78 and Dezful Embayment of the Zagros FAT Belt, and are believed to be of important implications
79 for structural interpretation of deep zones in FAT belts with double or multiple décollements and
80 prominent structural decoupling characteristics.

81

82 **2. Methodology**

83 **2.1. Fundamentals of the discrete element method**

84 The discrete element method is a particle-scale numerical method for modelling the bulk
85 mechanical behavior of a system comprised of an assembly of discrete particles (Cundall and
86 Strack, 1979). A single particle is treated as a rigid circular body that occupies a finite amount of
87 space. A discrete element model is composed of distinct particles that displace independently from
88 others, and elastically interact with their neighbouring particles at particle contacts using a soft

89 touch approach. The particle contact is defined as a linear spring in compression (Fig. 1) that resists
90 particle overlap, with the magnitude of particle overlap determined by the contact force via the
91 force-displacement law. The particles are allowed to be bonded together by applying interparticle
92 bonding at their contacts in order to resist both shear and extensional displacement. If either the
93 normal or shear bond strength is exceeded, the bond breaks, indicating the formation of
94 microfractures. Coalescence of adjacent microfractures leads to fracture propagation and
95 formation of macro scale fractures. Slip between particles that is resisted by a frictional strength
96 can occur between particles with unbonded contacts. The mechanical behaviour of a discrete
97 element system is characterised by movement of each particle and inter-particle forces acting at
98 particle contacts, which is governed by Newton's laws of motion. At all times, the forces acting
99 on any particle are exclusively determined by its interaction with the particles with which it is in
100 contact. The interaction of particles is regarded as a non-linear dynamic process with the states of
101 equilibrium developing whenever the internal forces balance.

102

103 The discrete element method was initially developed to investigate the mechanical behavior of a
104 granular media, which has been applied to soil and rock mechanics studies (Cundall and Strack,
105 1979). In recent year, the discrete element method has been effectively used for addressing
106 questions in structural geology and tectonics. In particular, this method has been successfully
107 adopted to simulate detachment fold (Hardy and Finch, 2005; Vidal-Royo et al., 2011), fold-related
108 fold (Finch et al., 2003, 2004; Cardozo et al., 2005; Hardy and Finch, 2006, 2007; Benesh et al.,
109 2007; Hughes et al., 2014; Hardy, 2018) and fold-and-thrust belt (Burbidge and Braun, 2002;
110 Naylor et al., 2005; Dean et al., 2013; Morgan, 2015; Meng and Hodgetts, 2019), and is thereby
111 considered to be an ideal method for the current study.

112

113 2.2. Model initial and boundary conditions

114 The Particle Flow Code (Cundall and Strack, 1999) software was employed to construct six series
115 of two-dimensional discrete element models. Each model consists of a 20 km long, rectangular-
116 shaped box filled with densely-packed circular particles (Fig. 1). All the models have a 150 m
117 thick basal décollement that comprises 12653 particles. Models 1-9 of series 1 have a thinner upper
118 décollement with a thickness of 75 m. Models 10-18 of series 4-6 have an equally thick upper
119 décollement to the basal décollement. The upper décollement in the models of series 1 and 4 have
120 the relatively shallowest burial depth, followed by models of series 2 and 5. Models of series 3 and
121 6 have the relatively deepest upper décollement. The stratigraphic units also contain eight
122 homogeneous layers that represent the bulk rock. Each layer is 150 m thick and contains 1580
123 particles. The colours assigned for the layers do not indicate mechanical contrasts, but are simply
124 used for bedding correlations.

125

126 The particle radii range from 5.0 to 10.0 m for the décollement layer (e.g. shale or salt), and 10.0
127 to 32.0 m for the bulk rock, both following a Gaussian distribution of particle size so as to inhibit
128 hexagonal close packing of particles. Particle density is 2100 kg/m³ for the décollement and 2600
129 kg/m³ for the bulk rock. Interparticle friction was prescribed to be 0.4 throughout the bonded
130 domain, and 0 within the décollements to ensure its low strength (Morgan, 2015).

131

132 The particle stiffness (normal and shear) of the bulk rock was set to be 1×10^7 N/m, which has
133 been effectively used to represent sedimentary rocks (Liu and Konietzky, 2018). A bonding
134 cohesion of 1.0, 2.5 and 5.0 MPa was prescribed to the three types of materials 1, 2 and 3. We then

135 performed numerical rock mechanics tests following the procedure described by Cundall and
136 Strack (1999), in order to derive the corresponding macroscopic mechanical parameters. In such
137 tests, synthetic rock samples were created and loaded in a strain-controlled fashion by displacing
138 the boundary walls at a sufficiently slow rate, so as to attain a quasistatic solution. The stresses
139 and strains experienced by the rock sample were determined in a macro-fashion by summing the
140 forces acting upon walls and tracking the relative distance between the walls. The test results reveal
141 that the Young's Modulus for the three types of materials is 21.14 MPa, whilst the unconfined
142 compressive strength (UCS) for materials 1, 2 and 3 is 1.87, 3.51 and 3.54 MPa, respectively.

143

144 The particles were packed by allowing randomly-generated particles to settle to the bottom of
145 model under gravitational force. The system was considered to have reached static equilibrium
146 when the mean unbalanced forces have been reduced to a negligible value. The particle assembly
147 was then trimmed to the desired thickness, which gave rise to a small amount of vertical elastic
148 rebound and surface uplift. This was followed by repeated trimming processes that allowed the
149 system to be settled (Benesh et al., 2007).

150

151 The three elastic walls served as the confined boundaries for the particle assembly, and the upper
152 surface was free. The left wall advanced at a controlled, uniform rate to the right, i.e. towards the
153 foreland direction, to yield horizontal shortening and tectonic deformation in the system (Fig. 1).

154 The models were gravitationally loaded by 1 g.

155

156 We present six snapshots of each model during the sequential shortening and deformation process,
157 to analyse their structural development. In particular, we focused on the features of structural

158 decoupling and their variances exhibited in different models, to gain insights into the dominant
159 controls.

160

161 **3. Results**

162 **3.1. Series 1**

163 **3.1.1. Model 1**

164 The modelling result of model 1 is characterised by successive formation of multiple short-
165 wavelength detachment folds that spread across the entire section (Fig. 2a). The first-order folds
166 individually consist of multiple second-order parasitic folds that exhibit a much smaller fold
167 wavelength and amplitude. The early-formed, symmetrical fold F1 is composed of two minor
168 disharmonic folds in the inner units that have a vergence toward the hinge zone, and grew by
169 consistent fold tightening with an increasing fold amplitude. F2 started to appear as a symmetric
170 detachment fold since T4, and continued to grow till T7. At T6, a forethrust began to be initiated
171 when the fold was right-verging, which was accompanied with a diapir rising from the basal
172 décollement. During T6 to T7, F2 evolved into a fault-propagation fold as a result of propagation
173 of the forethrust and a clock-wise rotation of its forelimb. Notably, the stratigraphic units above
174 and below the upper décollement exhibit a profound structural decoupling, which is represented
175 by the fact that the deep-seated folds barely propagated to the surface, and the superficial layer
176 remained largely planar.

177

178 The model accommodated crustal shortening mainly by thickening across the entire system (Table
179 1). The variances in crustal thickening result in a rather smooth downslope with a slope angle of
180 9.3° . The diapirs in model 1 are much shorter than those in other models in this series.

181

182 3.1.2. Model 2

183 The deformation structures formed in model 2 are characterised by three similar-sized box folds,
184 and five distinct diapirs originated from the basal decollement (Fig. 2b). Fold F1 was initiated as
185 a symmetrical box fold with oppositely dipping axial surfaces and a sub-vertical diapir as its core.
186 This was followed by the development of a minor fold F2 on the left of F1. Both folds continued
187 to grow until T4 when F3 and F4 were initiated. During this period, the fold axes of F1 exhibited
188 a slight clockwise rotation. F3 and F4 exhibited a right vergence during T4 to T6, which
189 constituted the inner disharmonic units of a larger fold. F5 began to develop at T6, and evolved
190 into a regularly-shaped box fold.

191

192 Structural decoupling commonly occurred, which is represented by the development of minor
193 disharmonic folds localised in the layers above the upper décollement. Such folds were developed
194 in the limbs of the deeply rooted folds as secondary structures, and significantly affect the surface
195 topography. The folds all propagated vertically to the surface, resulting in folding of the superficial
196 layers above the upper décollement. The diapirs exhibit a more distinct geometry and a larger size
197 than those in model 1 (Table 1). The accommodation of shortening was jointly achieved by vertical
198 fold growth and diapirism.

199

200 3.1.3. Model 3

201 The modelling result of model 3 is characterised by the formation of piggy-back thrusts (Fig. 2c).
202 Initially, F1 with disharmonic inner units were formed, which later developed into a fault-
203 propagation fold with a forethrust, and subsequently into a fault-bend fold. The hangingwall layers

204 were bent upward and transported passively along the ramp. F2 was formed at T4 and evolved into
205 a fault-propagation fold with a forethrust at T5. As shortening continued, the hangingwall layers
206 of the fault within F1 reached the backlimb of F2, resulting in a piggy-back arrangement of layers.
207 At T6, the diapir inside F2 rose up to the level of the upper décollement, and subsequently
208 propagated along the upper décollement. The persistent accumulation of displacement of the fault
209 within F2 led to the formation of a minor pop-up structure located in the front of F2.

210

211 Structural decoupling occurred at T4, when a fault-propagation fold with a backthrust was formed
212 in the superficial layers on the forelimb of F2. The pop-up structure formed in front of F2 caused
213 significant uplift and buckling of the superficial rocks. The result of model 3 exhibits a strong
214 strain localisation rather than distributed strain as shown in models 1 and 2. Horizontal shortening
215 was mainly accommodated by the development of forethrusts, whilst the foreland remained largely
216 undeformed (Table 1). This resulted in a dramatic uplift of the layers on the left of the model, and
217 a relatively steep downslope of 39.1° .

218

219 **3.2. Series 2**

220 **3.2.1. Model 4**

221 The deformation of model 4 is characterised by successive formation of multiple sinusoidal minor
222 detachment folds towards the foreland direction (Fig. 3a). Some folds contain second-order
223 parasitic folds developed in their limbs. The folds developed above and below the upper
224 décollement are approximately parallel, although significant differences appear locally.

225

226 The entire system has contributed to the accommodation of crustal shortening through thickening
227 (Table 1). This produced a gentle downslope with a slope angle of 8.3° . Compared to the other
228 two models in this series, model 4 exhibits the strongest structural decoupling.

229

230 **3.2.2. Model 5**

231 Model 5 successively produced three dominant asymmetric folds towards the foreland direction
232 (Fig. 3b). F1 was initiated at T2 as a detachment, diapir-cored fold and subsequently evolved into
233 a fault-propagation fold with a backthrust. The fold continued to grow from T2 to T5, which was
234 accompanied with the growth of its diapir. A forethrust was generated in its forelimb at T4. At T5,
235 a symmetric box fold F2 was initiated, which later became asymmetric by clockwise rotation of
236 its forelimb. F3 was formed at T6, and evolved into fault-propagation fold with a backthrust. In
237 this model, horizontal shortening was predominantly accommodated by folding and coeval
238 diapirism. The undeformed foreland is 2.33 km long (Table 1).

239

240 **3.2.3. Model 6**

241 Model 6 produced two imbricate thrusts with the hangingwall layers of the early-formed thrust
242 arranged as the first horse (Fig. 3c). F1 was initially formed at T3 as a diapir-cored, fault-
243 propagation fold with a forethrust, which later evolved into a fault-bend fold. The diapir reached
244 the surface at T4, and subsequently propagated in the sub-horizontal direction. F2 was formed on
245 the right of the model as a fault-bend fold with a backthrust at T6. The system accommodated
246 shortening mainly through fold vertical growth at the initial stage and accumulation of fault
247 displacement at the later stage. Deformation is largely localised to the piggyback thrusts, and the
248 unreformed foreland area reaches 5.26 km long (Table 1).

249

250 **3.3. Series 3**

251 **3.3.1. Model 7**

252 The modelling result of model 7 is characterised by successive formation of multiple short-
253 wavelength sinusoidal folds below the upper décollement and larger folds above the upper
254 décollement (Fig. 4a). The fold traces below and above the upper décollement are generally
255 parallel, although disharmonic folds below the upper décollement occur locally. However, the
256 amplitude and wavelength of the upper folds are much higher than the lower folds. The system
257 accommodated crustal shortening mainly by thickening (Table 1). The variances in crustal
258 thickening result in a downslope with a slope angle of 9.1° .

259

260 **3.3.2. Model 8**

261 Model 8 produced two dominant box folds and four diapirs during the shortening process (Fig.
262 4b). F1 was initially formed at T2 as a symmetric diapir-cored box fold, which became asymmetric
263 at T3 by anticlockwise rotation of the fold axial plane. Interestingly, the fold axial plane of F1
264 rotated clockwise with its diapir core dipping towards the hinterland direction. This was
265 accompanied with the formation of F2, a minor fold developed in the forelimb of F1. The diapir
266 within F2 was dipping oppositely to that within F1, i.e. towards the foreland. Meanwhile, F3 was
267 formed in the foreland as a fault-propagation fold with a backthrust. Later on, F1 and F2 had a
268 vergence towards the fold hinge. F4, a minor fault-propagation fold with a forethrust, was formed
269 in the forelimb of F3. Finally, F2 became merged with F1, and F4 merged with F3. Notably, F3
270 experienced a clockwise rotation of its axial plane. The system accommodated shortening mainly
271 by growth of the two dominant folds. The undeformed foreland is 4.46 km long (Table 1).

272

273 **3.3.3. Model 9**

274 The modelling result of model 9 is characterised by the formation of a single dominant fault-bend
275 fold in the foreland (Fig. 4c). Initially, the shortening was accommodated by uplifting and
276 overturning of the layers on the left, followed by the down-going leftmost segment being sliced
277 off the bulk rock during its clockwise rotation. At T4, F1 was initiated as a fault-propagation fold
278 with a backthrust. A diapir intruded upwards along the thrust fault. Later on, the diapir penetrated
279 through the upper décollement, accompanied with vertical growth of the fold and the hangingwall
280 layers being passively transported along the ramp. Multiple reverse faults were formed in the
281 forelimb of F1, i.e. hangingwall layers of the backthrust, during fold tightening. At T6, F1 passed
282 into a fault-bend fold as it continued to accumulated displacement. A tensile fracture was formed
283 in the fold hinge, and more reverse fractures were generated in the forelimb of F1. Following this,
284 F1 accommodated shortening by incremental growth in the vertical direction. The tensile fracture
285 in the fold hinge propagated downwards, with its aperture being enlarged.

286

287 Model 9 accommodated shortening mainly by vertical development of F1 and formation of
288 secondary structures within F1. The height of the diapir as the core of F1 is the highest among all
289 models (Table 1). The length of the unreformed foreland is longer than the other two models in
290 this series.

291

292 **3.4. Series 4**

293 **3.4.1. Model 10**

294 Generally, the modelling result of model 10 is rather similar to that of model 1, which is
295 characterised by successive formation of five dominant sinusoidal folds with numerous second-
296 order parasitic folds developed in the limbs of larger folds (Fig. 5a). A strong decoupling occurs
297 between the layers above and below the upper décollement. This is represented by the widespread
298 folding in the lower units, whilst the superficial layers remained flat and smooth. Crustal
299 thickening occurred throughout the system (Table 1), resulting in a downslope of 11.1° on the
300 surface. Multiple minor diapirs rose up from the basal décollement, with a maximum height of
301 0.51 km (Table 1).

302

303 **3.4.2. Model 11**

304 The modelling result of model 11 is characterised by the formation of three dominant detachment
305 fold and five diapirs (Fig. 5b). Initially, a minor fault-propagation fold with a forethrust was
306 generated above the upper décollement. A minor diapir originated from the basal décollement rose
307 up and led to the formation of F1 as an asymmetric box fold. Following this, a minor fault-
308 propagation fold with a backthrust was developed in the forelimb of F1 above the upper
309 décollement. Another diapir, close to the core of F1, was initiated ahead of F1 and caused gentle
310 folding of the upper layers. Later on, F1 and F2 constituted a larger fold through vergence towards
311 each other. At T4, two more folds F3 and F4 were formed as diapir-cored box folds. A fault-
312 propagation fold with a backthrust was generated in the forelimb of F3 above the upper
313 décollement. F3 and F4 merged into a larger fold at T6 that contains disharmonic inner units.
314 Meanwhile, F5 was formed as a rather symmetric box fold, whose fold limbs were later cut by
315 minor thrusts.

316

317 Model 11 accommodated shortening mainly through fold growth and diapirism. Notably, the
318 system exhibits a strong structural decoupling, which is represented by (1) the disharmonic folds
319 in the inner units of the first-order folds due to fold vergence; and (2) the secondary minor folds
320 and thrusts developed in the limbs of the deep-seated folds. The disharmonic folds significantly
321 increase the structural complexity of the system and the irregularity of the surface topography.

322

323 **3.4.3. Model 12**

324 The modelling result of model 12 is distinctively represented by the formation of piggyback thrusts
325 that exhibit a strong deformation localisation (Fig. 5c). Initially, thrust faults were nucleated on
326 the left of the model, with the hangingwall rocks being passively transported upwards along the
327 ramp. This process was repeated for the second thrust developed ahead of the first thrust. At T3,
328 F1 was formed as a fault-propagation fold that is associated with a hinterland-dipping diapir rising
329 from the basal décollement. As shortening continued, the hangingwall layers of the early thrusts
330 overrode the backlimb of F1, whilst the fold axes of F1 rotated clockwise. At T5, F1 evolved into
331 a fault-bend fold, and the hangingwall layers of the thrust in F1 were transported along the thrust
332 ramp towards the foreland direction. At the final stage, a fault-propagation fold F2 with a
333 backthrust was formed ahead of F1. Disharmonic minor fault-propagation folds were generated in
334 the limbs of F2. The accommodation of shortening was mainly achieved by the piggyback thrusts,
335 aided by the later fault-propagation fold.

336

337 **3.5. Series 5**

338 **3.5.1. Model 13**

339 The modelling result of model 13 is comparable to that of model 4, which is characterised by
340 successive formation of multiple sinusoidal detachment folds towards the foreland direction (Fig.
341 6a). The fold styles developed below and above the upper décollement exhibit variances, although
342 the fold traces are locally parallel. Crustal thickening occurred throughout the system (Table 1).
343 The variances in crustal thickening resulted in a downslope of the surface layer with a slope angle
344 of 9.5°.

345

346 **3.5.2. Model 14**

347 Model 14 produced three dominant box folds and four diapirs (Fig. 6b). F1 was initiated during
348 the rising up of a hinterland-dipping diapir from the basal décollement. This was accompanied
349 with the development of a fault-propagation fold cutting the layers in the forelimb of F1 above the
350 upper décollement. Later on, F1 experienced clockwise rotation of its forelimb and evolved into a
351 fault-propagation fold with a forethrust. At T4, a secondary fold was formed in the backlimb of
352 F1, with the development of a minor foreland-dipping diapir as its core. Following this, F2 was
353 formed as a rather symmetric box fold in the foreland, whose axial planes rotated clockwise and
354 caused F2 to become asymmetric at T6. F3 was then formed between F1 and F2 as a second order
355 detachment fold, followed by the formation of F4 in the foreland area ahead of F2. A hinterland-
356 dipping thrust fault was formed along the right axial trace of F4 in layers above the upper
357 décollement. The system accommodated shortening by forth and back folding of the layers,
358 coupled with development of thrusts within the folds. (Table 1).

359

360 **3.5.3. Model 15**

361 The modelling result of model 15 is characterised by in-sequence development of a fault-bend fold
362 and a fault-propagation fold (Fig. 6c). Initially, a fault-bend fold was developed on the leftmost
363 side of the model. The hangingwall fragment overrode the right layers, and became overturned as
364 shortening continued, prior to the formation of F1 at T3. F1, which was initially formed as a fault-
365 propagation fold with a forethrust, accumulated its reverse displacement and evolved into a fault-
366 bend fold when the thrust reached the surface. Notably, a tensile fracture occurred in the central
367 fold hinge and propagated downward. The diapir rooted in the basal décollement penetrated the
368 upper décollement at T4, which led to the anticlinal breakthrough at T7. F2 was formed at T7 as
369 a fault-propagation fold with a forethrust. A forethrust and backthrust developed in the backlimb
370 of F2 cut the layers above the upper décollement, resulting in a minor pop-up structure. The system
371 accommodated shortening mainly by fold development and also accumulation of reverse
372 displacement of F1. The undeformed area in the foreland is 5.41 km long (Table 1).

373

374 **3.6. Series 6**

375 **3.6.1. Model 16**

376 Model 16 successively produced a series of sinusoidal detachment folds towards the foreland
377 direction (Fig. 7a). The folds below the upper décollement exhibit a lower amplitude and
378 wavelength than the upper folds. Disharmonic folds occurred in layers above the upper
379 décollement as a result of vergence of neighbouring minor folds that constitute a larger fold. Other
380 than the disharmonic folds, the fold traces below and above the upper décollement are largely
381 parallel, and structural decoupling is less significant than that exhibited in model 10 and 13. Crustal
382 thickening occurred throughout the system (Table 1), which results in a downslope angle of 13.1°.

383

384 3.6.2. Model 17

385 The modelling result of model 17 is characterised by the formation of four dominant box folds and
386 seven diapirs (Fig. 7b). F1 was initially formed as a symmetric box fold with its core consisting of
387 a sub-vertical diapir. The fold became tightened as shortening continued, resulting in thrust faults
388 that propagated along both the fold axial traces. Later on, the axial plane of F1 had a clockwise
389 rotation, resulting in the asymmetric geometry of F1. This was accompanied with the growth of its
390 core diapir along the backthrust. Secondary folds were cut by reverse faults in the forelimb of F1.
391 F2 was initiated at T3, which evolved to become a fault-propagation fold with a backthrust at T4.
392 F2 then experienced tightening and a clockwise rotation with its core diapir steepened. During T4
393 and T5, two minor secondary folds F3 and F4 occurred on the left of F1 and F4, respectively. This
394 was followed by the development of F5 at T6, and F6 at T7, both of which are fault-propagation
395 fold with a forethrust. At T7 a minor diapir was initiated between F4 and F5, and caused gentle
396 folding of the host layer, whilst the layers above the upper décollement were not influenced.
397 Crustal shortening was mainly accommodated by in-sequence development of four dominant folds
398 and back-and-forth formation of some minor diapirs.

399

400 3.6.3. Model 18

401 Model 18 produced a concave-up pop-up structure that consists of an early-formed fault-
402 propagation fold with a backthrust, and a later fault-bend fold with a forethrust (Fig. 7c). The
403 geometry of the pop-up structure is similar to that described by Alsop et al. (2017). F1 was initiated
404 at T2 as a fault-propagation fold, and its fold axis subsequently experienced a clockwise rotation.
405 Notably, its core diapir penetrated the upper décollement at T4, whilst the forelimb of F1 was cut
406 by a thrust fault developed along the axial trace. At T5, F2 was formed with the diapir intruding

407 upward along the forethrust. A backthrust was developed along fold axial trace when F2 became
408 tightened as shortening continued. At T7, F2 evolved into a fault-bend fold as it accumulated
409 reverse displacement, with a tensile fracture occurring in its hinge zone. Interestingly, F1 and F2
410 converged towards each other, which finally constituted a pop-up structure. The system
411 accommodated shortening mainly by the pop-up structure, which is tightly associated with
412 development of the two major thrusts. The undeformed area is 5.16 km long in the foreland (Table
413 1).

414

415 **3.7. Summary of modelling results**

416 **3.7.1. Models with the same mechanical property**

417 Models that are composed of the least competent material 1, exhibit similar structural styles, which
418 are characterised by multiple short-wavelength, sinusoidal detachment folds (Fig. 8). The diapirs
419 rooted in the basal décollement are much smaller than those in models composed of more
420 competent materials. Shortening of the system resulted in crustal thickening across the entire
421 section, resulting in a clear taper towards the foreland direction. Models that are composed of more
422 competent material 2, all produced diapir-cored box folds. The diapirs in these folds are often
423 inclined, resulting in an overall asymmetric fold geometry. The fold limbs are commonly faulted.
424 Models that are composed of the most competent material 3, are dominated by thrusts, fault-bend
425 folds and pop-up structures. Strain localisation, represented by piggyback arrangement of
426 forethrust and progressive accumulation of fault displacement during shortening, is distinct.
427 Tensile fractures commonly occurred in fold hinge zones.

428

429 Structural decoupling between stratigraphic units above and below the upper décollement is the
430 most profound in models composed of the least competent material 1, followed by those composed
431 of more competent material 2. Models that are composed of the most competent material 3 exhibit
432 the least features of structural decoupling.

433

434 **3.7.2. Models with the same depth of the upper décollement**

435 Models with the shallowest upper décollement exhibit the most significant structural decoupling
436 above and below the upper décollement (Fig. 8). This is represented by the fact that the underlying,
437 deep-rooted structures did not significantly affect the upper layers in models 1 and 10 with
438 incompetent materials, and also represented by minor disharmonic folds and reverse faults
439 developed above the upper décollement in other models. Pop-up structures that only occurred in
440 the upper units also contributed to structural decoupling. Structural decoupling is much less
441 common in models with a deeper upper décollement.

442

443 **3.7.3. Models with the same thickness of the upper décollement**

444 Generally, models (10-18) with equally thick décollements exhibit a more significant structural
445 decoupling below and above the upper décollements (Fig. 8). Moreover, a thicker upper
446 décollement tends to hinder vertical propagation of folds, and to promote lateral development of
447 structures. This is evident by a larger number of folds and diapirs developed in models with an
448 equally thick upper décollement to the basal décollement than models with a thinner upper
449 décollement.

450

451 **4. Discussion**

452 This section is focused on the discussion of the controls of rock mechanical property, depth and
453 thickness of the upper décollement on structural styles and decoupling in FAT belts, followed by
454 a comparison of the modelling results to the Zagros FAT belt that contains multiple décollements.

455

456 **4.1. Controls on structural styles**

457 The final configuration of the thin-skinned fold belts produced in our models is represented by the
458 formation of sinusoidal detachment folds, box folds, fault-propagation folds, fault-bend folds, pop-
459 up structures, tensile fractures and piggyback thrusts (Fig. 8). Given the predefined boundary and
460 initial conditions of the six series of models, it is possible to evaluate the geologic controls on the
461 competing mechanisms of folding versus faulting versus diapirism that gave rise to the styles of
462 deformation in the systems.

463

464 Each series of models, with the same boundary and initial conditions except bonding cohesion,
465 exhibit significantly different structural styles, which can be represented by (1) models with the
466 least competent material are dominated by short-wavelength, sinusoidal and disharmonic
467 detachment folds; (2) models with a more competent material are dominated by faulted, diapir-
468 cored box folds; and (3) models with the most competent material are dominated by thrusts, fault-
469 bend folds and tensile fractures. This indicates that rock mechanical property plays a dominant
470 role in controlling structural styles, agreeing with Morgan (2015) and Meng and Hodgetts (2019).

471

472 Depth of the upper décollement is tightly associated with the fold-dominated systems, where a
473 deeper upper décollement favours a shorter wavelength of the folds developed below the
474 décollement. Oppositely, a shallower upper décollement allows the deep-seated folds in the lower

475 units to grow vertically and to attain a larger wavelength. For systems dominated by thrusts,
476 structural styles are also significantly influenced by the depth of the upper décollement, i.e. a
477 shallower upper décollement promotes transportation of hangingwall layers along the ramps of
478 piggyback forethrusts through accumulation of fault displacement, whilst a deeper upper
479 décollement favours formation of backthrusts (Fig. 4c) or a combination of backthrusts and
480 forethrusts (model 18) (Fig. 7c) to accommodate shortening.

481

482 The different modelling results of models with varied upper décollement thickness suggest that
483 the thickness of the upper décollement is one of the factors that determined the structures produced
484 within the systems. Such differences may be attributed to the fact that the upper décollement
485 separates the upper units from the lower units and hindered vertical growth of folds by
486 redistribution of weak décollement materials onto synclines. Moreover, a thicker upper
487 décollement is more likely to cause the formation of minor structures in the upper units, e.g. fault-
488 propagation folds and pop-up structures, especially in systems with a shallow upper décollement.
489 This is possible because that flow of weak materials and the resulting thickness variation is more
490 common in a thicker upper décollement during shortening, which can support fold development
491 by material redistribution into fold cores as suggested by Stewart (1996).

492

493 **4.2. Controls on structural decoupling**

494 Our modelling results reveal that the models composed of the least competent material, exhibit the
495 most significant structural decoupling above and below the upper décollement. This is represented
496 by the fact that folds were formed disharmonically above the below the upper décollement (Fig.
497 8). Moreover, such materials promoted forward propagation of deformation and a more distributed

498 strain rather than vertical growth of existing structures, which resulted in crustal thickening across
499 the entire section (Table 1). The simple surface structures mask complex folds at depth. Conversely,
500 models that are composed of more competent materials promoted vertical growth of structures and
501 strain localisation. This favoured parallel folding in the upper and lower units, and hence
502 contributed to structural coupling.

503

504 Another major control on structural decoupling is the depth of the upper décollement. The
505 modelling results presented indicate that a shallow upper décollement favours the formation of
506 minor parasitic structures in the limbs of deep-seated folds with a broad wavelength, and also pop-
507 up structures in the superficial layers. Differently, traces of folds above and below the upper
508 décollement tend to be more parallel if the upper décollement is deeper. Hence, the shallower the
509 upper décollement is, the higher the degree of structural decoupling will become.

510

511 Thickness of the upper décollement also played an important role in structural decoupling in our
512 models. It is shown that a thicker upper décollement inhibited the upward growth of folds either
513 through local thinning of the décollement layer on top of anticline hinge zones, or thickening above
514 fold limbs (Fig. 5a). Moreover, a thicker upper décollement provided sufficient materials to fill
515 cores of disharmonic folds formed above the upper décollement during material redistribution (Fig.
516 5b). Such features are much less distinctive in models with a thinner upper décollement.

517

518 **4.3. Comparison to the Zagros Fold-and-Thrust Belt**

519 Although the models presented are not aimed for directly simulating structures of any natural
520 prototypes, here it is attempted to compare the modelling results to the Zagros FAT Belt with

521 multidécollements. The Zagros FAT Belt is a NW-SE-trending, 1800 km long segment of the
522 Alpine-Himalayan orogenic belt (Fig. 9a), which has been extensively studied not only because
523 that it is one of the most active collisional belts worldwide (Sella et al., 2002; Pirouz et al., 2017),
524 but also due to its specular fold trains developed in a thick multilayer of Paleozoic to Cenozoic
525 sediments that serve as the host to one of the world's largest hydrocarbon provinces (Cooper, 2007).
526 There are three prominent décollement levels within the sedimentary sequence, including the
527 Hormuz Formation, the Dashtak Formation and the Gashsaran Formation, which significantly
528 affected the mechanical stratigraphy and rock rheology profile of the Zagros FAT Belt (Sepehr et
529 al., 2006) (Fig. 9). The Early Cambrian Hormuz evaporites serves as the basal décollement for the
530 fold trains to be detached on (Bahroudi and Koyi, 2003). The middle Miocene evaporites of the
531 Gashsaran Formation constitute a relatively shallow upper décollement in the Dezful area (Fig. 9b)
532 (Ghanadian et al., 2017b). The Triassic evaporites of the Dashtak Formation is one of the major
533 intermediate décollements in coastal Fars and southwestern Izeh (Fig. 11b) (Najafi et al., 2014).
534 The three major décollements significantly affected the mechanical stratigraphy and rock rheology
535 profile of Zagros (Sepehr et al., 2006) (Fig. 9b).

536

537 In the Zagros FAT Belt, most of the shortening of the sedimentary cover has been accommodated
538 by multilayer detachment folding and Hormuz salt diapirism (Motamedi et al., 2011; Yamato et
539 al., 2011; Najafi et al., 2018). The Gachsaran evaporites have been suggested to have enabled
540 decoupling the surface structures and the deep-seated folds in areas where the evaporites act as the
541 upper décollement (Sherkati et al., 2005; Fard et al., 2006, 2011; Mouthereau et al., 2007;
542 Ghanadian et al., 2017b; Derikvand et al., 2018, 2019; Najafi et al., 2018) (Fig. 9b). Structural
543 decoupling is represented by (1) flow of mobile salt onto underlying synclines (Sherkati and

544 Letouzey, 2004; Ghanadian et al., 2017a); (2) formation of strongly disharmonic, short-wavelength
545 detachment folds above the Gachsaran Formation (Fig. 9c); and (3) termination of some deep-
546 seated thrust faults that encounter the Gachsaran evaporites, and development of minor thrust
547 faults that are originated from the Gachsaran Formation (Ghanadian et al., 2017b). Notably,
548 structural decoupling controlled by the Gachsaran evaporites becomes less considerable in the NE
549 sector compared to the SW sector of Deful, due to the decrease in its thickness (Derikvand et al.,
550 2018). The conclusions drawn above largely agree with our modelling results that a shallower and
551 thicker upper décollement contributes to a more profound structural decoupling, especially to the
552 generation of secondary disharmonic folds and thrusts in the shallow strata that do not coincide
553 with the deep-seated structures (Figs 2b, 5b).

554

555 The Triassic evaporites of the Dashtak Formation is identified as the main intermediate
556 décollement that effectively shaped the folds in the Fars region (Fig. 9b). The folds developed
557 there mainly include asymmetric faulted box folds. Notably, the fold traces in strata below and
558 above the Dashtak evaporites are approximately parallel, indicating a less degree of structural
559 decoupling than that in the Dezful Embayment. The relatively 'simple' structural styles in the Fars
560 (Blanc et al., 2003) are similar to our modeling results of models 5 and 14 with an intermediate-
561 depth upper décollement. In particular, structural decoupling in the two models is less significant
562 than models with a shallower upper décollement.

563

564 It should be noted that the numerical models presented are highly simplified and only show the
565 first order structural similarities to the Zagros FAT Belt. To better reproduce the structures

566 developed in this area, it is suggested that future models should incorporate more comprehensive
567 regional geological data.

568

569 **5. Conclusions**

570 This study uses the discrete element method to simulate thin-skinned tectonic deformation in
571 stratigraphic sequences with double décollements, to yield new insights into the combined control
572 of rock competence, depth and thickness of the upper décollement on structural styles and
573 decoupling characteristics. We conclude the following:

574

575 (1) The models with double décollements and varying parameters produced a range of
576 structural styles as the result of shortening, including sinusoidal detachment folds in models
577 composed of the least competent material, faulted and diapir-cored box folds in models
578 composed of a more competent material, and thrust-dominated piggyback thrust systems
579 and pop-up structures in models composed of the most competent material.

580

581 (2) Structural decoupling above and below the upper décollements decreases as rock
582 competence increases. A shallower upper décollement favours the development of minor
583 disharmonic folds and pop-up structures as second-order structures that do not coincide
584 with the deep-seated folds. A thicker upper décollement contributes to the generation of
585 more disharmonic minor folds in the shallow strata by providing sufficient mobile
586 materials to fill fold cores, and remobilization of materials onto synclines, both enhancing
587 structural decoupling.

588

589 (3) Our modeling results exhibit first-order structural similarities to the predominant diapir-
590 cored box folds in the Zagros Fold-and-Thrust Belt with multidécollements.

591

592 (4) This study demonstrates that rock competence, depth and thickness of the upper
593 décollement can jointly influence thin-skinned tectonics in systems with multiple
594 décollement levels, and determine the degree of structural decoupling.

595

596 **Acknowledgements**

597 The first author's position is funded by the Sandstone Injection Research Group (SIRG)
598 consortium. Itasca is thanked for technical support. Google Earth™ is acknowledged for providing
599 satellite images.

600

601 **References**

602 Alsop, G.I., Marco, S., Weinberger, R., Levi, T., 2017. Upslope-verging back thrusts developed
603 during downslope-directed slumping of mass transport deposits. *Journal of Structural*
604 *Geology* 100, 45-61.

605 Bahroudi, A., Koyi, H., 2003. Effect of spatial distribution of Hormuz salt on deformation style in
606 the Zagros fold and thrust belt: an analogue modelling approach. *Journal of the*
607 *Geological Society* 160, 719-733.

608 Benesh, N.P., Plesch, A., Shaw, J.H., Frost, E.K., 2007. Investigation of growth fault bend folding
609 using discrete element modeling: Implications for signatures of active folding above blind
610 thrust faults. *Journal of Geophysical Research: Solid Earth* 112, B03S04,
611 doi:10.1029/2006JB004466.

- 612 Blanc, E.-P., Allen, M.B., Inger, S., Hassani, H., 2003. Structural styles in the Zagros simple folded
613 zone, Iran. *Journal of the Geological Society* 160, 401-412.
- 614 Bonini, M., 2003. Detachment folding, fold amplification, and diapirism in thrust wedge
615 experiments. *Tectonics* 22, 1065, doi:10.1029/2002TC001458.
- 616 Borderie, S., Graveleau, F., Witt, C., Vendeville, B.C., 2018. Impact of an interbedded viscous
617 décollement on the structural and kinematic coupling in fold-and-thrust belts: Insights
618 from analogue modeling. *Tectonophysics* 722, 118-137.
- 619 Burbidge, D.R., Braun, J., 2002. Numerical models of the evolution of accretionary wedges and
620 fold-and-thrust belts using the distinct-element method. *Geophysical Journal
621 International* 148, 542-561.
- 622 Callot, J.-P., Trocmé, V., Letouzey, J., Albouy, E., Jahani, S., Sherkati, S., 2012. Pre-existing salt
623 structures and the folding of the Zagros Mountains. *Geological Society, London, Special
624 Publications* 363, 545-561.
- 625 Cardozo, N., Allmendinger, R.W., Morgan, J.K., 2005. Influence of mechanical stratigraphy and
626 initial stress state on the formation of two fault propagation folds. *Journal of Structural
627 Geology* 27, 1954-1972.
- 628 Casciello, E., Vergés, J., Saura, E., Casini, G., Fernández, N., Blanc, E., Homke, S., Hunt, D.W.,
629 2009. Fold patterns and multilayer rheology of the Lurestan Province, Zagros simply
630 folded belt (Iran). *Journal of the Geological Society* 166, 947-959.
- 631 Chapple, W.M., 1978. Mechanics of thin-skinned fold-and-thrust belts. *Geological Society of
632 America Bulletin* 89, 1189-1198.
- 633 Cooper, M., 2007. Structural style and hydrocarbon prospectivity in fold and thrust belts: a global
634 review. *Geological Society, London, Special Publications* 272, 447-472.

- 635 Cundall, P.A., Strack, O.D.L., 1979. A discrete numerical model for granular assemblies.
636 Geotechnique 29, 47-65.
- 637 Cundall, P.A., Strack, O.D.L., 1999. Particle flow code in 2 dimensions. Itasca consulting group,
638 Inc.
- 639 Davis, D.M., Engelder, T., 1985. The role of salt in fold-and-thrust belts. Tectonophysics 119, 67-
640 88.
- 641 Dean, S.L., Morgan, J.K., Fournier, T., 2013. Geometries of frontal fold and thrust belts: Insights
642 from discrete element simulations. Journal of Structural Geology 53, 43-53.
- 643 Derikvand, B., Alavi, S.A., Fard, I.A., Hajjalibeigi, H., 2018. Folding style of the Dezful
644 Embayment of Zagros Belt: Signatures of detachment horizons, deep-rooted faulting and
645 syn-deformation deposition. Marine and Petroleum Geology 91, 501-518.
- 646 Derikvand, B., Alavi, S.A., Fard, I.A., Jalali, L., 2019. Changing in fold geometry from faulted
647 detachment fold to fault-bend fold, a case study: The Zeloï Anticline in the Dezful
648 Embayment, southwest of Iran. Journal of Petroleum Science and Engineering 173, 381-
649 401.
- 650 Driehaus, L., Nalpas, T., Ballard, J.-F., 2014. Interaction between deformation and sedimentation
651 in a multidecollement thrust zone: Analogue modelling and application to the Sub-
652 Andean thrust belt of Bolivia. Journal of Structural Geology 65, 59-68.
- 653 Erickson, S.G., 1996. Influence of mechanical stratigraphy on folding vs faulting. Journal of
654 Structural Geology 18, 443-450.
- 655 Fard, I.A., Braathen, A., Mokhtari, M., Alavi, S.A., 2006. Interaction of the Zagros Fold-Thrust
656 Belt and the Arabian-type, deep-seated folds in the Abadan Plain and the Dezful
657 Embayment, SW Iran. Petroleum Geoscience 12, 347-362.

- 658 Fard, I.A., Sepehr, M., Sherkati, S., 2011. Neogene salt in SW Iran and its interaction with Zagros
659 folding. *Geological Magazine* 148, 854-867.
- 660 Farzipour-Saein, A., Yassaghi, A., Sherkati, S., Koyi, H., 2009. Mechanical stratigraphy and
661 folding style of the Lurestan region in the Zagros Fold–Thrust Belt, Iran. *Journal of the*
662 *Geological Society* 166, 1101-1115.
- 663 Farzipour-Saein, A., Koyi, H., 2016. Intermediate decollement activation in response to the basal
664 friction variation and its effect on folding style in the Zagros fold-thrust belt, an analogue
665 modeling approach. *Tectonophysics* 687, 56-65.
- 666 Feng, L., Bartholomew, M.J., Choi, E., 2015. Spatial arrangement of décollements as a control on
667 the development of thrust faults. *Journal of Structural Geology* 75, 49-59.
- 668 Finch, E., Hardy, S., Gawthorpe, R., 2003. Discrete element modelling of contractional fault-
669 propagation folding above rigid basement fault blocks. *Journal of Structural Geology* 25,
670 515-528.
- 671 Finch, E., Hardy, S., Gawthorpe, R., 2004. Discrete-element modelling of extensional fault-
672 propagation folding above rigid basement fault blocks. *Basin Research* 16, 467-488.
- 673 Gee, E.R., Gee, D.G., 1989. Overview of the geology and structure of the Salt Range, with
674 observations on related areas of northern Pakistan. *Geological Society of America Special*
675 *Papers* 232, 95-112.
- 676 Ghanadian, M., Faghieh, A., Fard, I.A., Kusky, T., Maleki, M., 2017a. On the role of incompetent
677 strata in the structural evolution of the Zagros Fold-Thrust Belt, Dezful Embayment, Iran.
678 *Marine and Petroleum Geology* 81, 320-333.

- 679 Ghanadian, M., Faghih, A., Fard, I.A., Grasemann, B., Soleimany, B., Maleki, M., 2017b. Tectonic
680 constraints for hydrocarbon targets in the Dezful Embayment, Zagros Fold and Thrust
681 Belt, SW Iran. *Journal of Petroleum Science and Engineering* 157, 1220-1228.
- 682 Ghanadian, M., Faghih, A., Grasemann, B., Fard, I.A., Maleki, M., 2017c. Analogue modeling of
683 the role of multi-level decollement layers on the geometry of orogenic wedge: an
684 application to the Zagros Fold–Thrust Belt, SW Iran. *International Journal of Earth
685 Sciences* 106, 2837-2853.
- 686 Ghazian, R.K., Buiter, S.J.H., 2014. Numerical modelling of the role of salt in continental collision:
687 an application to the southeast Zagros fold-and-thrust belt. *Tectonophysics* 632, 96-110.
- 688 Hardy, S., Finch, E., 2005. Discrete-element modelling of detachment folding. *Basin Research* 17,
689 507-520.
- 690 Hardy, S., Finch, E., 2006. Discrete element modelling of the influence of cover strength on
691 basement-involved fault-propagation folding. *Tectonophysics* 415, 225-238.
- 692 Hardy, S., Finch, E., 2007. Mechanical stratigraphy and the transition from trishear to kink-band
693 fault-propagation fold forms above blind basement thrust faults: a discrete-element study.
694 *Marine and Petroleum Geology* 24, 75-90.
- 695 Hardy, S., 2018. Discrete element modelling of extensional, growth, fault-propagation folds. *Basin
696 Research*, doi: 10.1111/bre.12335.
- 697 Hughes, A.N., Benesh, N.P., Shaw, J.H., 2014. Factors that control the development of fault-bend
698 versus fault-propagation folds: Insights from mechanical models based on the discrete
699 element method (DEM). *Journal of Structural Geology* 68, 121-141.
- 700 Izquierdo-Llavall, E., Roca, E., Xie, H., Pla, O., Muñoz, J.A., Rowan, M.G., Yuan, N., Huang, S.,
701 2018. Influence of Overlapping décollements, Syntectonic Sedimentation, and Structural

- 702 Inheritance in the Evolution of a Contractional System: The Central Kuqa Fold-and-
703 Thrust Belt (Tian Shan Mountains, NW China). *Tectonics* 37, 2608-2632.
- 704 Jahani, S., Hassanpour, J., Mohammadi-Firouz, S., Letouzey, J., de Lamotte, D.F., Alavi, S.A.,
705 Soleimany, B., 2017. Salt tectonics and tear faulting in the central part of the Zagros Fold-
706 Thrust Belt, Iran. *Marine and Petroleum Geology* 86, 426-446.
- 707 Jaumé, S.C., Lillie, R.J., 1988. Mechanics of the Salt Range-Potwar Plateau, Pakistan: A fold-
708 and-thrust belt underlain by evaporites. *Tectonics* 7, 57-71.
- 709 Leturmy, P., Mugnier, J.L., Vinour, P., Baby, P., Colletta, B., Chabron, E., 2000. Piggyback basin
710 development above a thin-skinned thrust belt with two detachment levels as a function of
711 interactions between tectonic and superficial mass transfer: the case of the Subandean
712 Zone (Bolivia). *Tectonophysics* 320, 45-67.
- 713 Liu, Y., Konietzky, H., 2018. Particle-Based Modeling of Pull-Apart Basin Development.
714 *Tectonics* 37, 343-358.
- 715 Massoli, D., Koyi, H.A., Barchi, M.R., 2006. Structural evolution of a fold and thrust belt
716 generated by multiple décollements: analogue models and natural examples from the
717 Northern Apennines (Italy). *Journal of Structural Geology* 28, 185-199.
- 718 McQuarrie, N., 2004. Crustal scale geometry of the Zagros fold–thrust belt, Iran. *Journal of*
719 *Structural Geology* 26, 519-535.
- 720 Meng, Q., Hodgetts, D., 2019. Combined control of décollement layer thickness and cover rock
721 cohesion on structural styles and evolution of fold belts: A discrete element modelling
722 study. *Tectonophysics* 757, 58-67.

- 723 Morgan, J.K., 2015. Effects of cohesion on the structural and mechanical evolution of fold and
724 thrust belts and contractional wedges: Discrete element simulations. *Journal of*
725 *Geophysical Research: Solid Earth* 120, 3870-3896.
- 726 Motamedi, H., Sepehr, M., Sherkati, S., Pourkermani, M., 2011. Multi-phase Hormuz salt
727 diapirism in the southern Zagros, SW Iran. *Journal of Petroleum Geology* 34, 29-43.
- 728 Motamedi, H., Sherkati, S., Sepehr, M., 2012. Structural style variation and its impact on
729 hydrocarbon traps in central Fars, southern Zagros folded belt, Iran. *Journal of Structural*
730 *Geology* 37, 124-133.
- 731 Mouthereau, F., Tensi, J., Bellahsen, N., Lacombe, O., De Boisgrollier, T., Kargar, S., 2007.
732 Tertiary sequence of deformation in a thin-skinned/thick-skinned collision belt: The
733 Zagros Folded Belt (Fars, Iran). *Tectonics* 26, TC5006, doi:10.1029/2007TC002098.
- 734 Najafi, M., Yassaghi, A., Bahroudi, A., Vergés, J., Sherkati, S., 2014. Impact of the Late Triassic
735 Dashtak intermediate detachment horizon on anticline geometry in the Central Frontal
736 Fars, SE Zagros fold belt, Iran. *Marine and Petroleum Geology* 54, 23-36.
- 737 Najafi, M., Vergés, J., Etemad-Saeed, N., Karimnejad, H.R., 2018. Folding, thrusting and
738 diapirism: Competing mechanisms for shaping the structure of the north Dezful
739 Embayment, Zagros, Iran. *Basin Research* 30, 1200-1229.
- 740 Naylor, M., Sinclair, H.D., Willett, S., Cowie, P.A., 2005. A discrete element model for orogenesis
741 and accretionary wedge growth. *Journal of Geophysical Research: Solid Earth* 110,
742 B12403, doi:10.1029/2003JB002940.
- 743 Pirouz, M., Avouac, J.-P., Hassanzadeh, J., Kirschvink, J.L., Bahroudi, A., 2017. Early Neogene
744 foreland of the Zagros, implications for the initial closure of the Neo-Tethys and
745 kinematics of crustal shortening. *Earth and Planetary Science Letters* 477, 168-182.

- 746 Ruh, J.B., Kaus, B.J.P., Burg, J.P., 2012. Numerical investigation of deformation mechanics in
747 fold-and-thrust belts: Influence of rheology of single and multiple décollements.
748 *Tectonics* 31, TC3005,doi:10.1029/2011TC003047.
- 749 Ruh, J.B., Gerya, T., Burg, J.-P., 2017. Toward 4D modeling of orogenic belts: Example from the
750 transpressive Zagros Fold Belt. *Tectonophysics* 702, 82-89.
- 751 Schori, M., Mosar, J., Schreurs, G., 2015. Multiple detachments during thin-skinned deformation
752 of the Swiss Central Jura: a kinematic model across the Chasseral. *Swiss Journal of*
753 *Geosciences* 108, 327-343.
- 754 Sella, G.F., Dixon, T.H., Mao, A., 2002. REVEL: A model for recent plate velocities from space
755 geodesy. *Journal of Geophysical Research: Solid Earth* 107, NO. B4, 2081,
756 10.1029/2000JB000033.
- 757 Sepehr, M., Cosgrove, J., Moieni, M., 2006. The impact of cover rock rheology on the style of
758 folding in the Zagros fold-thrust belt. *Tectonophysics* 427, 265-281.
- 759 Sherkati, S., Letouzey, J., 2004. Variation of structural style and basin evolution in the central
760 Zagros (Izeh zone and Dezful Embayment), Iran. *Marine and petroleum geology* 21, 535-
761 554.
- 762 Sherkati, S., Molinaro, M., de Lamotte, D.F., Letouzey, J., 2005. Detachment folding in the Central
763 and Eastern Zagros fold-belt (Iran): salt mobility, multiple detachments and late basement
764 control. *Journal of Structural Geology* 27, 1680-1696.
- 765 Sherkati, S., Letouzey, J., Frizon de Lamotte, D., 2006. Central Zagros fold-thrust belt (Iran): New
766 insights from seismic data, field observation, and sandbox modeling. *Tectonics* 25,
767 TC4007, doi:10.1029/2004TC001766.

- 768 Sommaruga, A., 1999. Décollement tectonics in the Jura forelandfold-and-thrust belt. Marine and
769 Petroleum Geology 16, 111-134.
- 770 Stewart, S.A., 1996. Influence of detachment layer thickness on style of thin-skinned shortening.
771 Journal of Structural Geology 18, 1271-1274.
- 772 Stewart, S. A., 1999. Geometry of thin-skinned tectonic systems in relation to detachment layer
773 thickness in sedimentary basins. Tectonics 18, 719-732.
- 774 Tavani, S., Cifelli, F., 2010. Deformation pattern analysis and tectonic implications of a
775 décollement level within the Central Apennines (Italy). Geological Journal 45, 582-596.
- 776 Vergés, J., Goodarzi, M.G.H., Emami, H., Karpuz, R., Efstathiou, J., Gillespie, P., 2011. Multiple
777 detachment folding in Pusht-e Kuh arc, Zagros: Role of mechanical stratigraphy. AAPG
778 Memoir 94, 69-94.
- 779 Vidal-Royo, O., Hardy, S., Muñoz, J.A., 2011. The roles of complex mechanical stratigraphy and
780 syn-kinematic sedimentation in fold development: insights from discrete-element
781 modelling and application to the Pico del Águila anticline (External Sierras, Southern
782 Pyrenees). Geological Society, London, Special Publications 349, 45-60.
- 783 Wang, X., Guan, J.S.S., Hubert-Ferrari, A., Jia, R.G.-M.C., 2011. Cenozoic structure and tectonic
784 evolution of the Kuqa fold belt, southern Tianshan, China. AAPG Memoir 94, 215-243.
- 785 Yamato, P., Kaus, B.J.P., Mouthereau, F., Castellort, S., 2011. Dynamic constraints on the crustal-
786 scale rheology of the Zagros fold belt, Iran. Geology 39, 815-818.

Table 1. Summary of modelling results of the discrete element models.

| Model series | Number | Relative depth of the upper décollement | Relative thickness of the upper décollement | Number of diapirs | Max. diapir height (km) | Surface uplift (km) | | Length of undeformed foreland (km) | Structural styles | Distinct structural decoupling, Y/N |
|--------------|--------|---|---|-------------------|-------------------------|---------------------|------|------------------------------------|---|-------------------------------------|
| | | | | | | Min. | Max. | | | |
| S1 | 1 | shallow | thinner | 8 | 0.48 | 1.13 | 1.63 | 0 | sinusoidal folds, box folds, | Y |
| | 2 | shallow | thinner | 4 | 1.13 | 0 | 1.79 | 2.20 | box fold | Y |
| | 3 | shallow | thinner | 3 | 1.36 | 0 | 3.10 | 5.67 | piggyback thrusts | Y |
| S2 | 4 | intermediate | thinner | 8 | 0.37 | 0.30 | 1.87 | 0 | sinusoidal folds, box folds, | Y |
| | 5 | intermediate | thinner | 4 | 1.49 | 0 | 1.85 | 2.33 | box folds, fault-propagation folds | N |
| | 6 | intermediate | thinner | 4 | 1.89 | 0 | 2.75 | 5.26 | piggyback thrusts, fault-bend folds | N |
| S3 | 7 | deep | thinner | 11 | 0.42 | 0.29 | 1.82 | 0 | sinusoidal folds | Y |
| | 8 | deep | thinner | 3 | 1.59 | 0 | 1.72 | 4.46 | box fold, fault-propagation fold | N |
| | 9 | deep | thinner | 1 | 2.94 | 0 | 2.49 | 6.04 | fault-bend fold, tensile fractures | N |
| S4 | 10 | shallow | equal | 7 | 0.51 | 0.27 | 1.84 | 0 | box folds, sinusoidal folds | Y |
| | 11 | shallow | equal | 6 | 1.09 | 0 | 1.93 | 1.87 | box folds | Y |
| | 12 | shallow | equal | 2 | 1.66 | 0 | 4.68 | 5.37 | piggyback thrusts, fault-propagation fold | Y |
| S5 | 13 | intermediate | equal | 8 | 0.35 | 0.27 | 1.85 | 0 | sinusoidal folds, box folds | Y |
| | 14 | intermediate | equal | 4 | 1.44 | 0 | 1.95 | 2.24 | box folds | N |
| | 15 | intermediate | equal | 2 | 2.11 | 0 | 3.15 | 5.41 | fault-propagation and bend folds, tensile fractures | N |
| S6 | 16 | deep | equal | 5 | 0.37 | 0.24 | 2.11 | 0 | sinusoidal folds, box folds | Y |
| | 17 | deep | equal | 3 | 1.56 | 0 | 1.99 | 1.13 | box folds, fault-propagation folds | N |
| | 18 | deep | equal | 2 | 1.93 | 0 | 2.91 | 5.16 | fault-propagation and bend folds, tensile fractures | N |

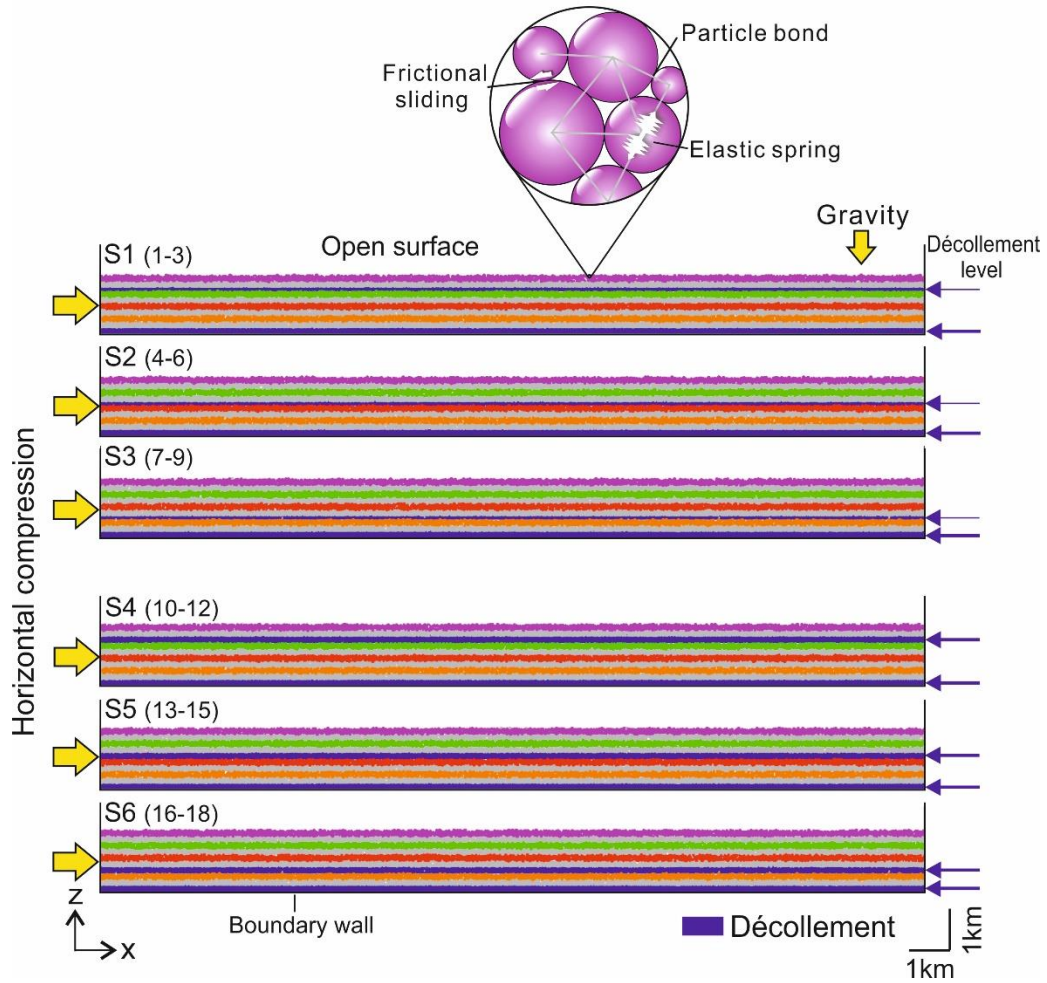


Fig. 1. (a) Design and boundary conditions of the discrete element models. Models of series 1-3 contain a thinner upper décollement than the basal décollement. Models of series 4-6 contain two equally thick décollements. The enlarged circular area shows particle interactions.

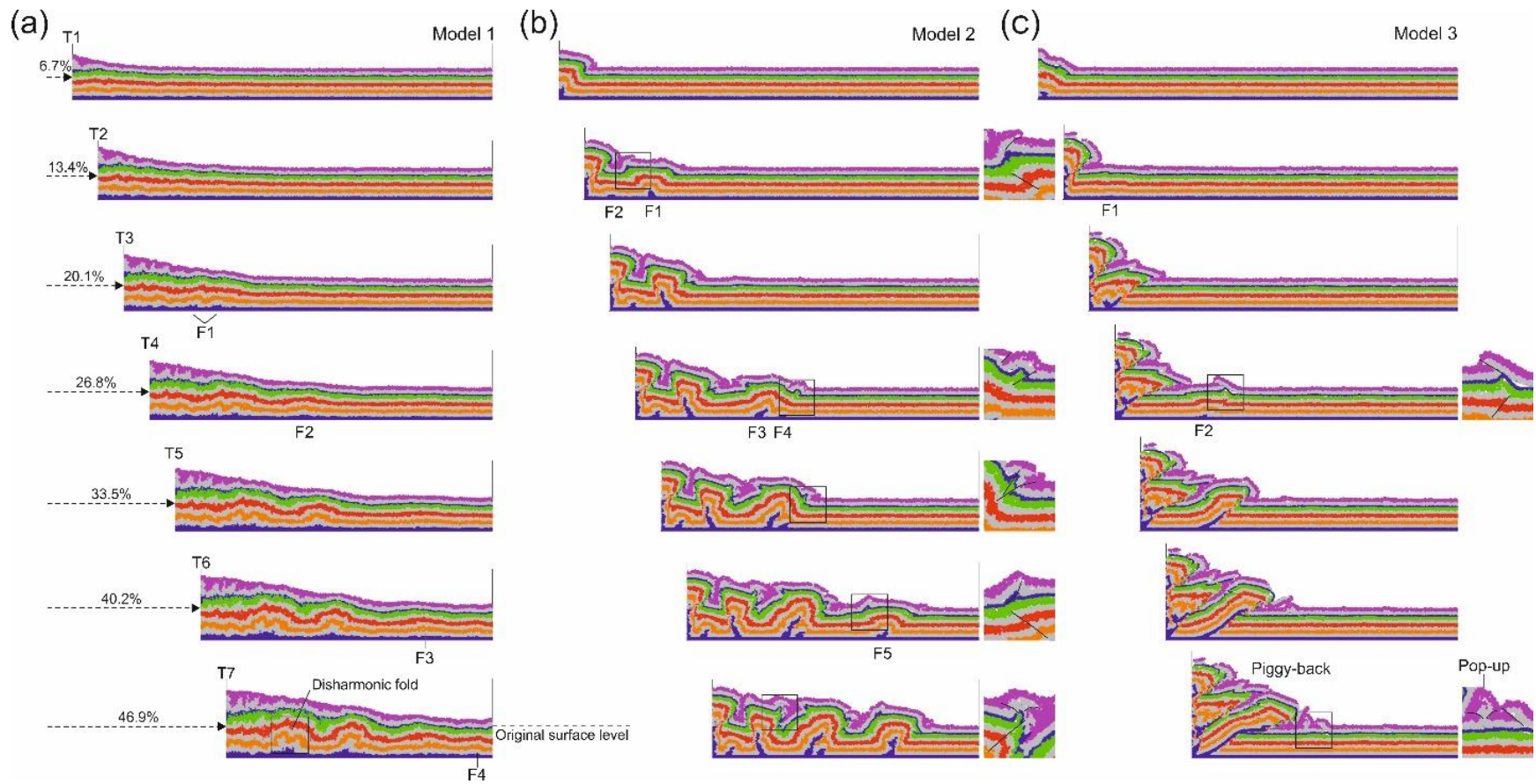


Fig. 2. Modelling results of model 1 (a), model 2 (b) and model 3 (c) in series 1. The enlarged boxes show features of structural decoupling above and below the upper décollement.

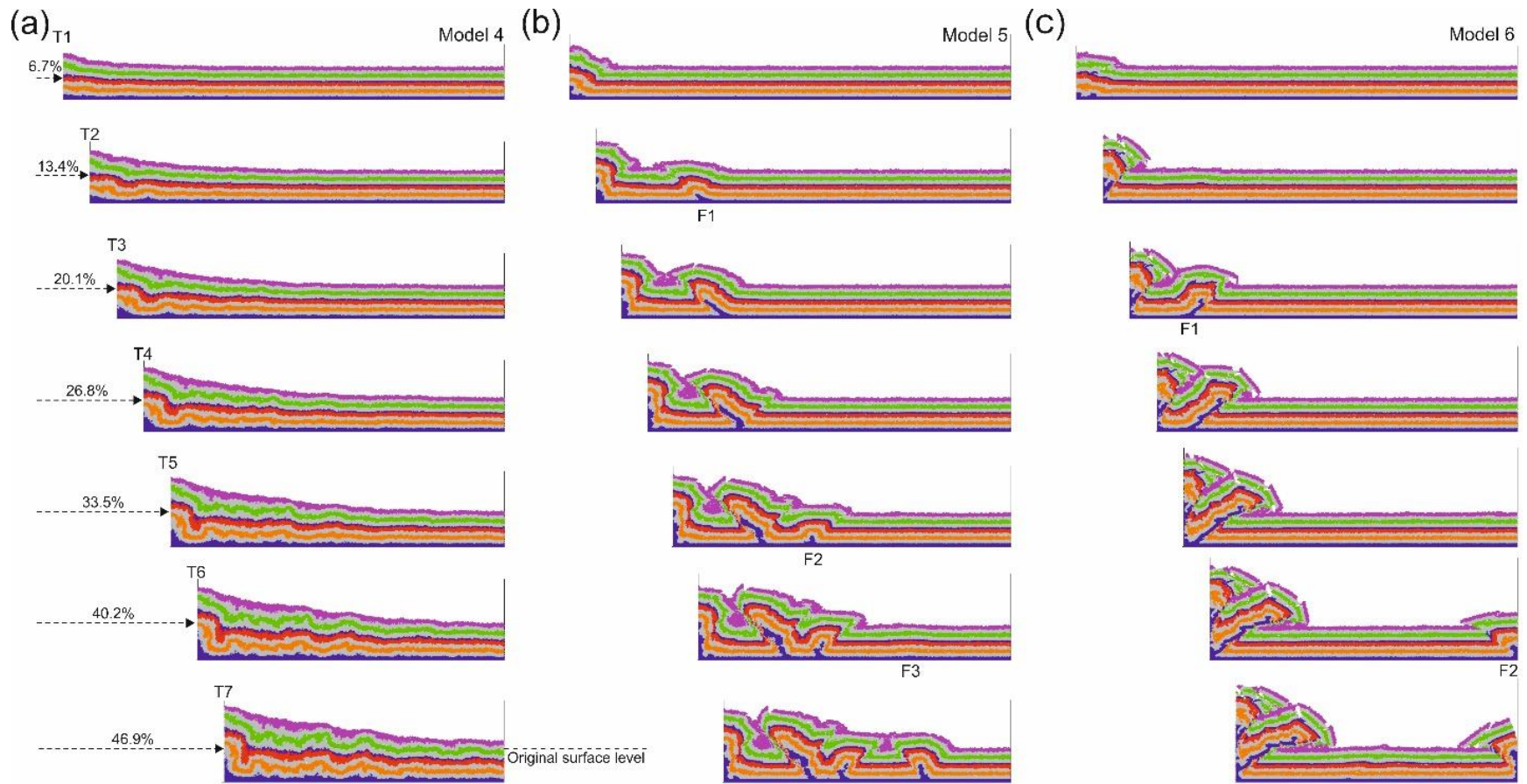


Fig. 3. Modelling results of model 4 (a), model 5 (b) and model 6 (c) in series 2.

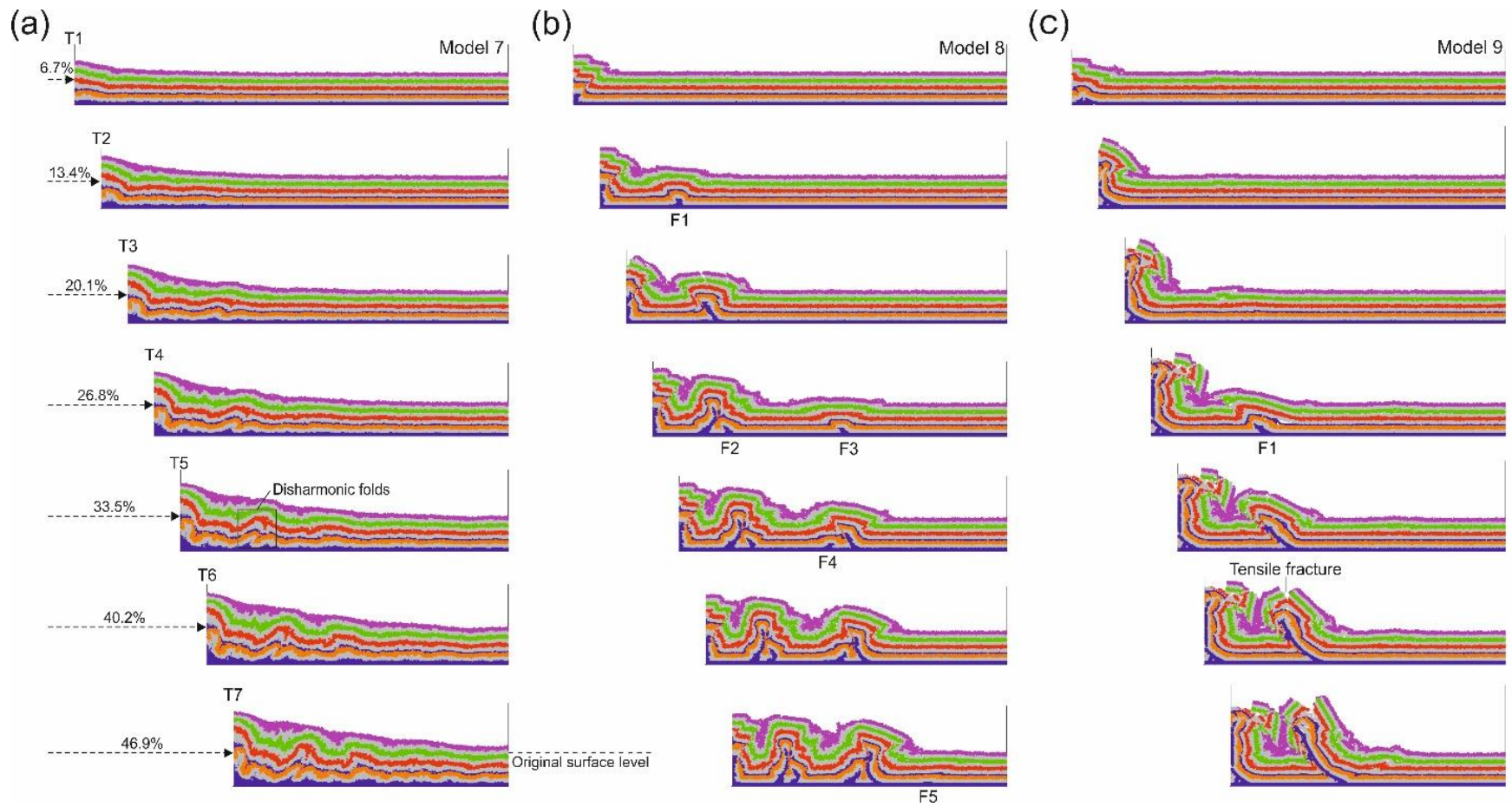


Fig. 4. Modelling results of model 7 (a), model 8 (b) and model 9 (c) in series 3.

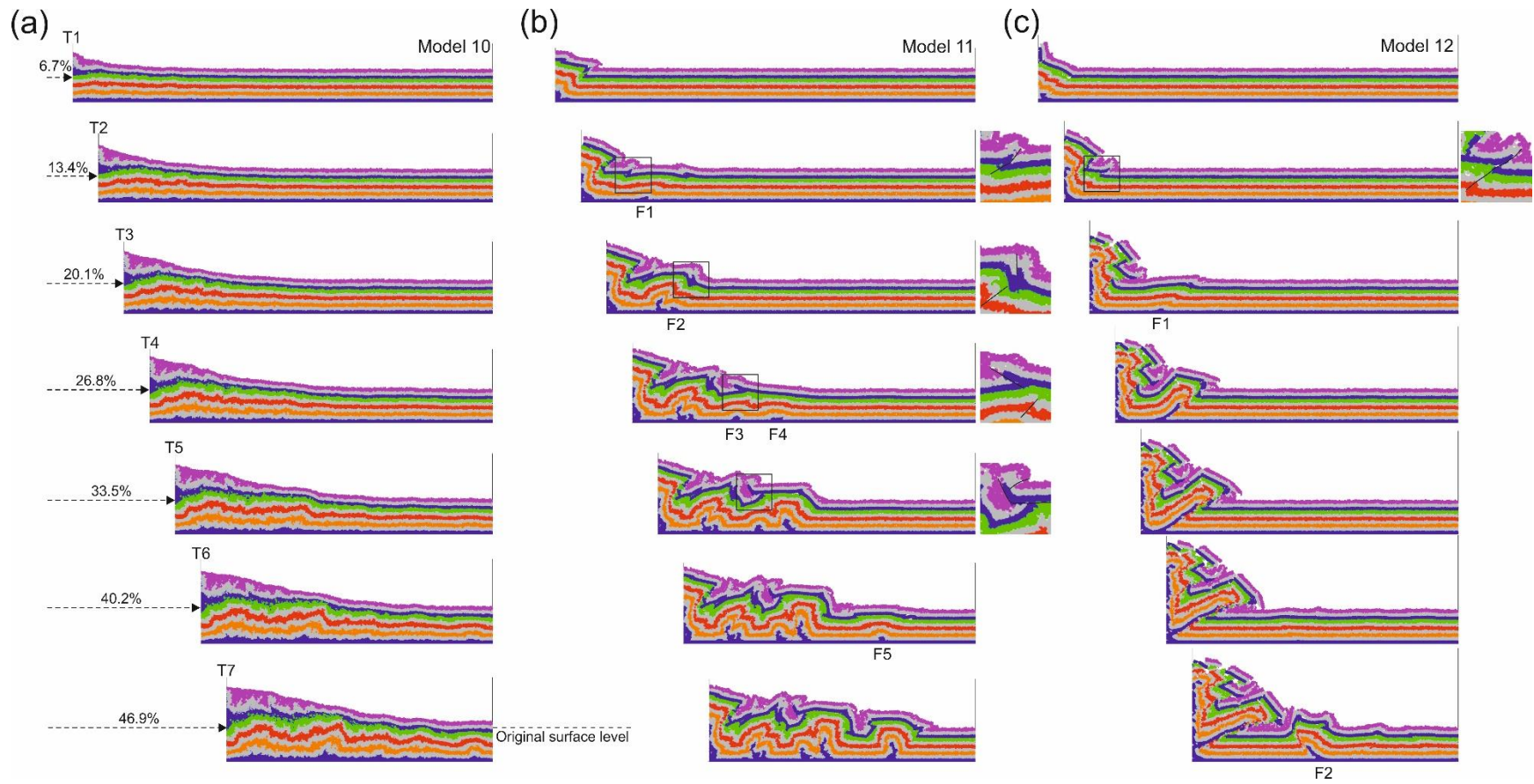


Fig. 5. Modelling results of model 10 (a), model 11 (b) and model 12 (c) in series 4. The enlarged boxes show features of structural decoupling above and below the upper décollement.

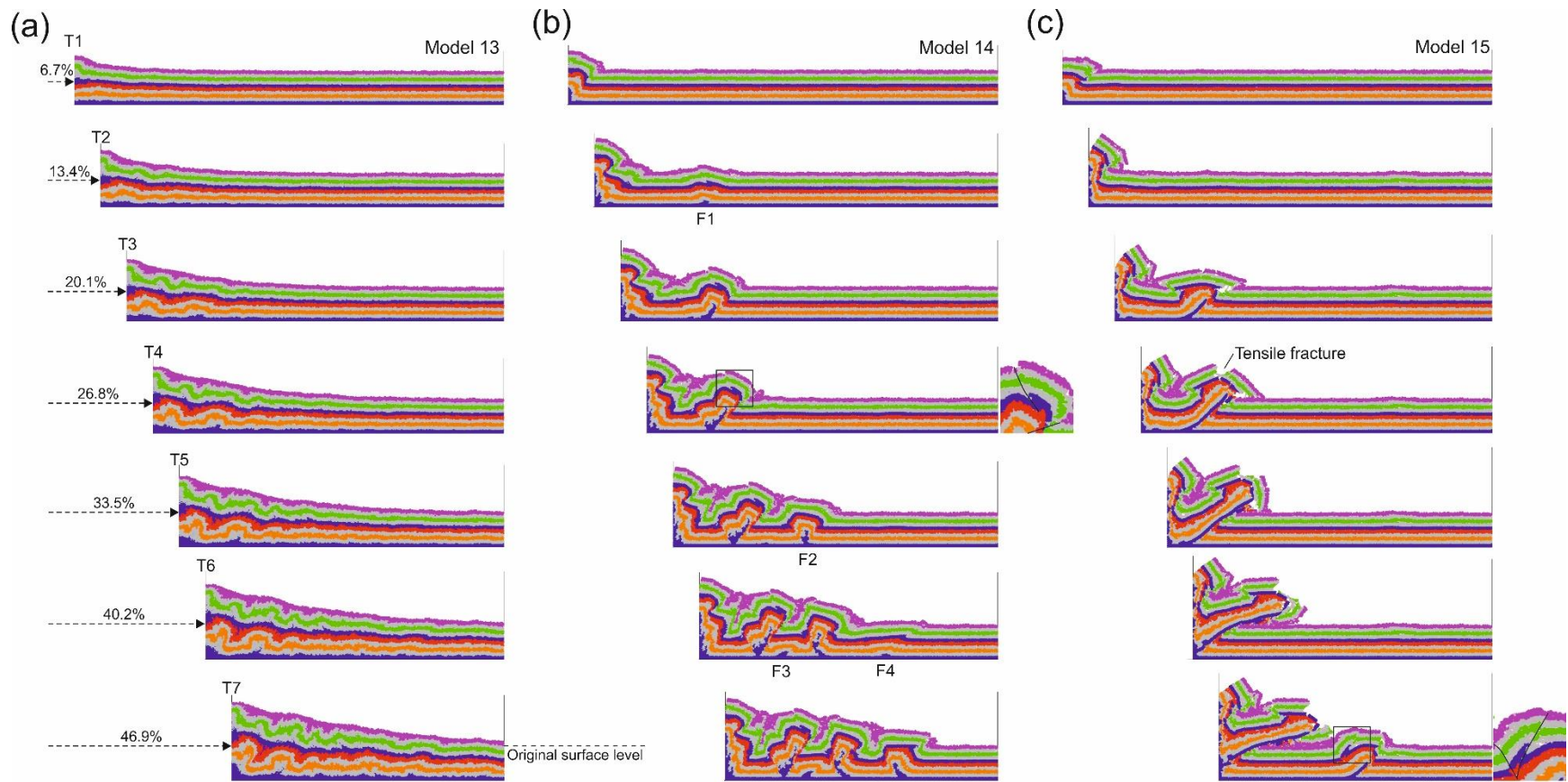


Fig. 6. Modelling results of model 13 (a), model 14 (b) and model 15 (c) in series 5. The enlarged boxes show features of structural decoupling above and below the upper décollement.

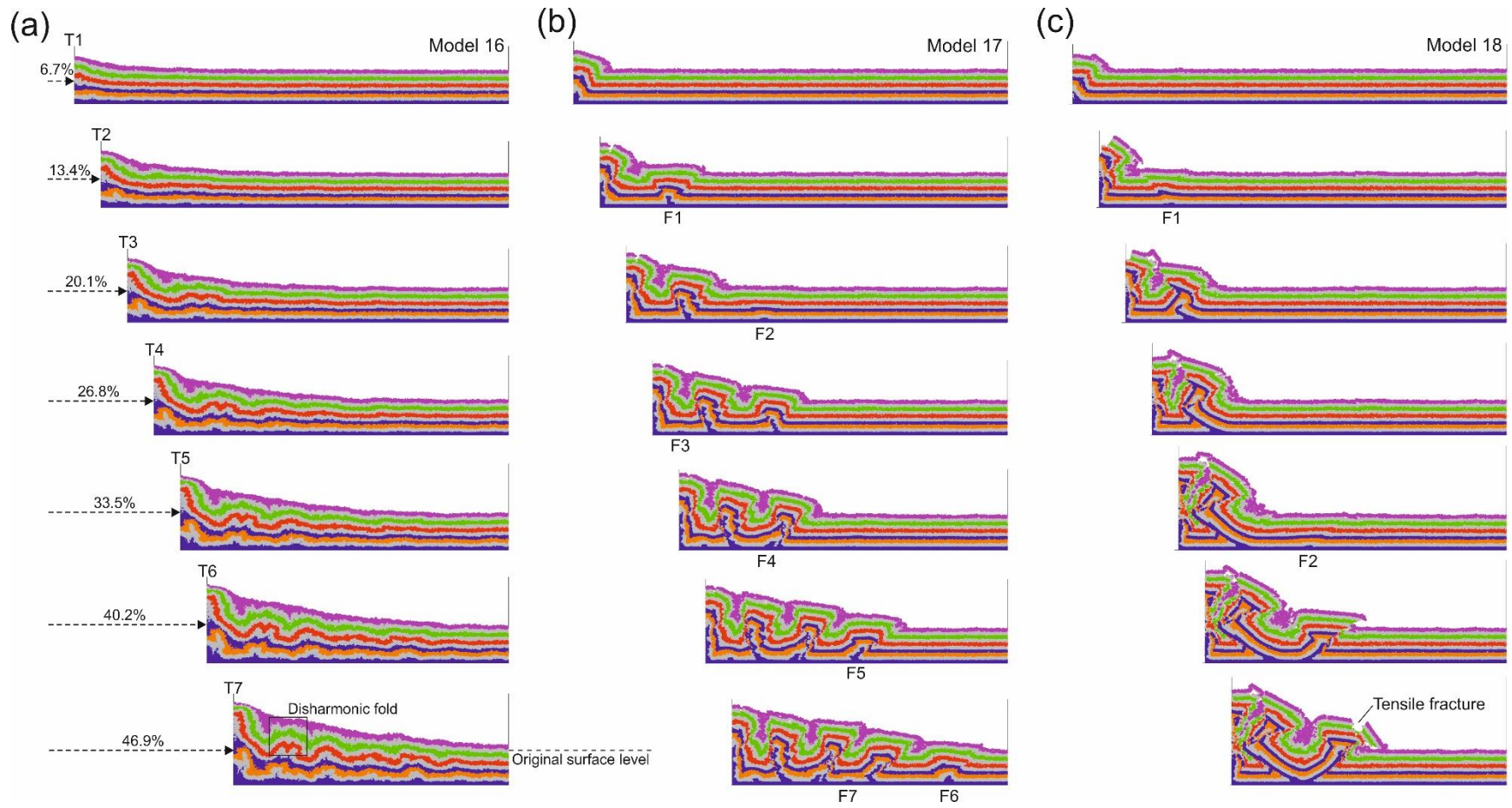


Fig. 7. Modelling results of model 16 (a), model 17 (b) and model 18 (c) in series 6.

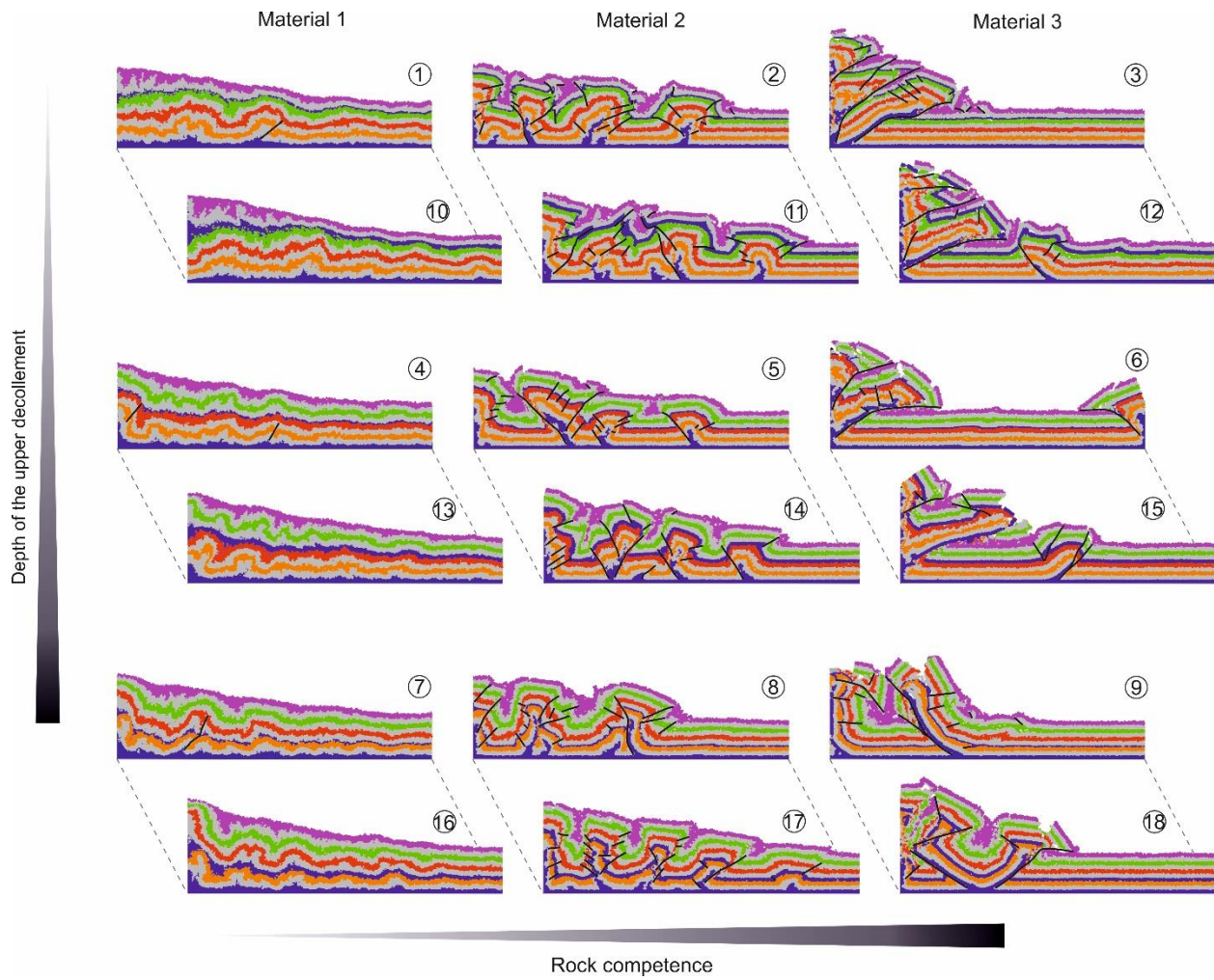


Fig. 8. Summary of modelling results of all models. Fault traces are highlighted by black solid lines.

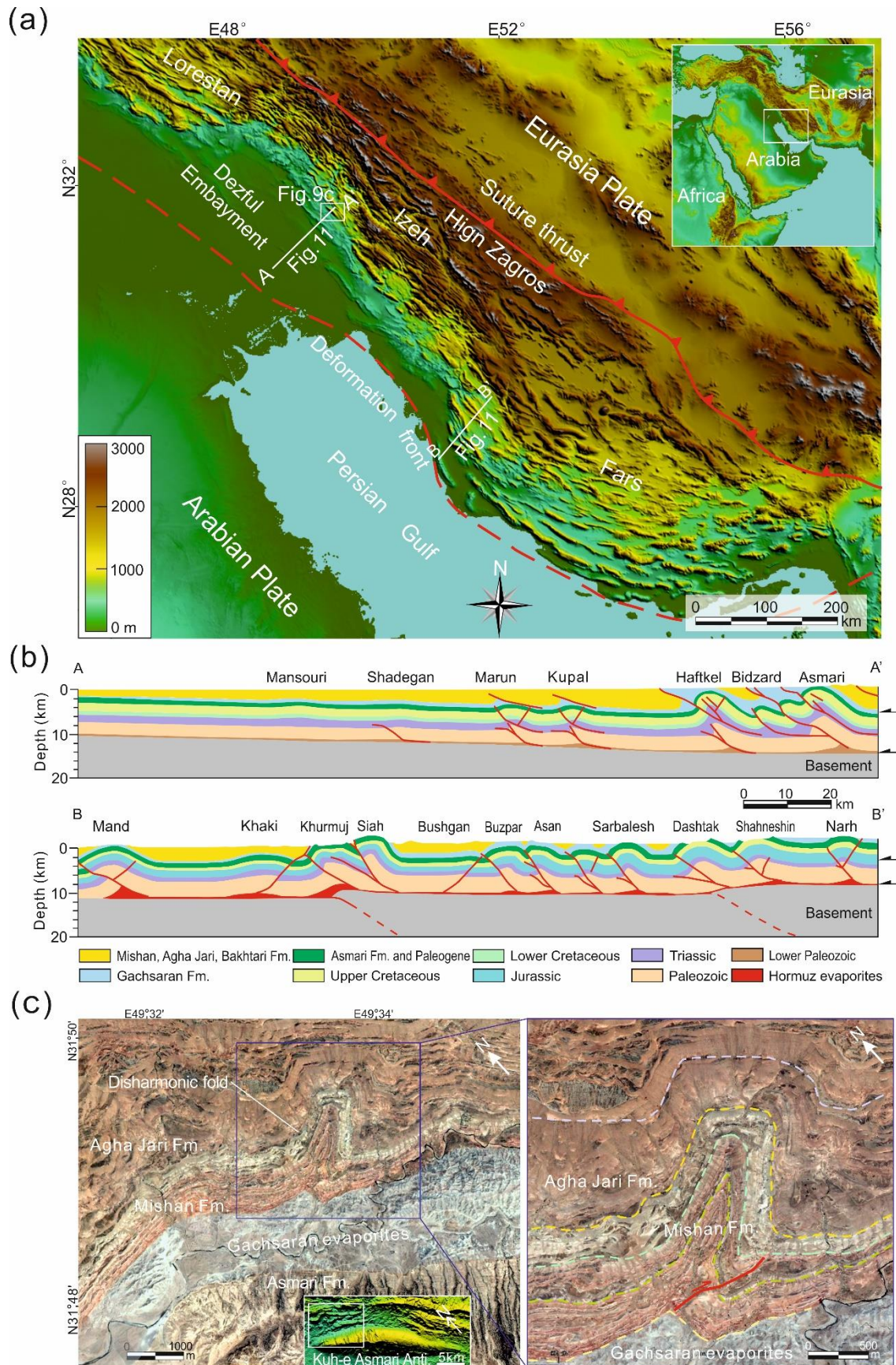


Fig. 9. (a) Elevation map showing the location and main structural elements of the Zagros Fold-and-Thrust Belt. (b) Cross sections of the Dezful Embayment and the Fars province. Modified from Sherkati et al (2006). See locations in Fig. 9a. (c) Google satellite image showing outcrop exposure of a minor disharmonic fold developed above the shallow Gachsaran evaporites in the Kuh-e Asmari Anticline. The image is located in the box area of the elevation map that shows the fold geometry. The enlarged box shows details of the disharmonic fold. The dashed lines highlight the bedding traces as markers for correlation. The reverse fault is marked by the red line. See location in Fig. 9a.